RESEARCH ARTICLE



Volumetric particle tracking velocimetry (PTV) uncertainty quantification

Sayantan Bhattacharya¹ · Pavlos P. Vlachos¹

Received: 27 November 2019 / Revised: 6 May 2020 / Accepted: 22 July 2020 / Published online: 18 August 2020 © Springer-Verlag GmbH Germany, part of Springer Nature 2020

Abstract

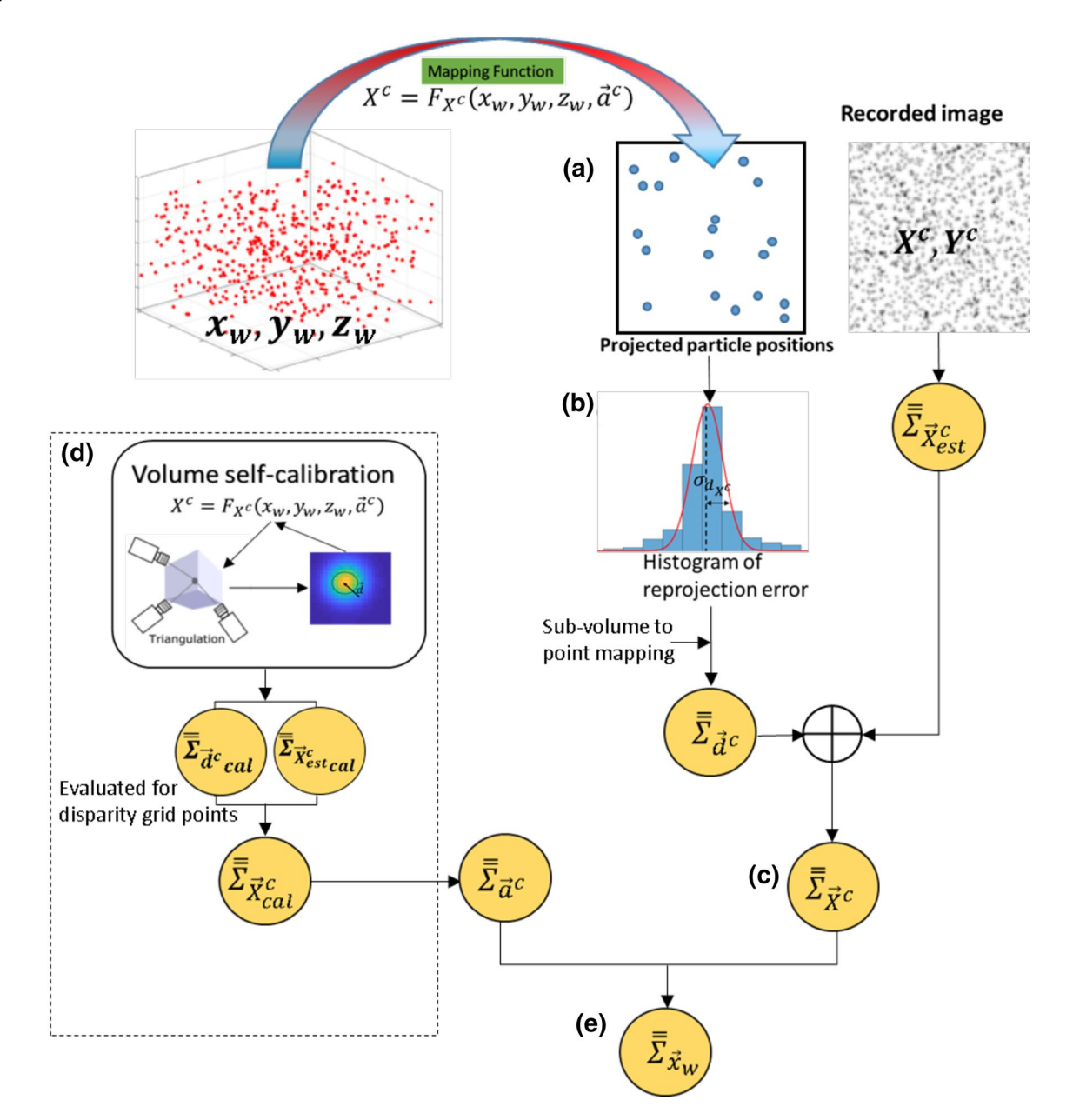
We introduce the first comprehensive approach to determine the uncertainty in volumetric Particle Tracking Velocimetry (PTV) measurements. Volumetric PTV is a state-of-the-art non-invasive flow measurement technique, which measures the velocity field by recording successive snapshots of the tracer particle motion using a multi-camera set-up. The measurement chain involves reconstructing the three-dimensional particle positions by a triangulation process using the calibrated camera mapping functions. The non-linear combination of the elemental error sources during the iterative self-calibration correction and particle reconstruction steps increases the complexity of the task. Here, we first estimate the uncertainty in the particle image location, which we model as a combination of the particle position estimation uncertainty and the reprojection error uncertainty. The latter is obtained by a gaussian fit to the histogram of disparity estimates within a sub-volume. Next, we determine the uncertainty in the camera calibration coefficients. As a final step, the previous two uncertainties are combined using an uncertainty propagation through the volumetric reconstruction process. The uncertainty in the velocity vector is directly obtained as a function of the reconstructed particle position uncertainty. The framework is tested with synthetic vortex ring images. The results show good agreement between the predicted and the expected RMS uncertainty values. The prediction is consistent for seeding densities tested in the range of 0.01–0.1 particles per pixel. Finally, the methodology is also successfully validated for an experimental test case of laminar pipe flow velocity profile measurement where the predicted uncertainty in the streamwise component is within 9% of the RMS error value.



Pavlos P. Vlachos pvlachos@purdue.edu

Department of Mechanical Engineering, Purdue University, West Lafayette, USA

Graphic abstract



N

Abbreviations

 F_{X^c}, F_{Y^c}

 $\vec{x}_w = \{x_w y_w z_w\}$ World coordinates or physical

 $\vec{X}^c = \{X^c Y^c\}$ coordinates

Camera ima

Camera image coordinates for camera c X^c And Y^c calibration mapping function

 $\vec{a}^c = \left\{a_i^c\right\}_{i=1to19} \quad \begin{array}{l} \text{for camera } c \\ \text{Camera } c \text{ ma} \end{array}$

Camera c mapping function coefficient

error in variable p

Standard uncertainty in variable p

 $\overline{\Sigma}_p$ Covariance matrix in variable p

Number of cameras

 N_{cal} Number of disparity grid points

 $\vec{d} = \{d_{X^c}d_{Y^c}\}$ Disparity vector estimated from ensemble of reprojection error for each camera

 \boldsymbol{c}

u, v, w Velocity components in x, y, z direc-

tions, respectively

|p| L²-norm or magnitude of a variable p



$\overline{\overline{C}}_{ec{x}_w}$	Coefficient matrix of mapping function gradients with respect to \vec{x}_w for all
_	cameras
$\overline{C}_{\overline{a}^c}$	Coefficient matrix of mapping function gradients with respect to \vec{a}^c evaluated at disparity grid points
$ ho_{pq}$	Correlation coefficient between variables p and q
\vec{x}_{wj}	The world coordinates at j th time frame where j is an integer
$\sigma_{res}^2 = \frac{diagA}{diagA}$	Variance in fit residual error
$diag\overline{A}$	A function which denotes the diagonal
	elements of matrix $\frac{=}{A}$

Subscripts

b	Related to the measure of bias error or
	uncertainty in any variable

cal A variable or quantity evaluated in the

calibration process

est Denotes the estimated value of any

variable

true Denotes the known or designed value

of any variable

Acronyms

PIV Particle Image Velocimetry
PTV Particle Tracking Velocimetry
IPR Iterative Particle Reconstruction
OTF Optical Transfer Function

STB Shake-The-Box

CRLB Cramer Rao Lower Bound

ppp Particles per pixel

1 Introduction

Volumetric PTV (Maas et al. 1993; Baek and Lee 1996; Ohmi and Li 2000; Pereira et al. 2006) is a fluid velocity measurement technique which resolves the three-dimensional (3D) flow structures by tracking the motion of tracer particles introduced in the flow. The tracer particle motion is recorded with multiple cameras to obtain projected particle images. Each camera is also linked to the physical space using a calibration mapping function (Soloff et al. 1997). The particle images are then mapped back to the physical space using a triangulation process (Maas et al. 1993; Wieneke 2008). Finally, a three-dimensional (3D) tracking of the reconstructed particles estimates the Lagrangian trajectories of the particles and subsequently resolves the volumetric velocity field. PTV easily lends itself to calculation of particle acceleration from the tracked trajectories. Also, unlike Tomographic Particle Image Velocimetry (Tomo-PIV) (Elsinga et al. 2006), which involves spatial averaging over the interrogation volume, 3D PTV yields a vector for every tracked particle position leading to a higher vector density. However, as the number of particles increases, identification of overlapping particles and its corresponding 3D reconstruction becomes challenging, which leads to a trade-off between spatial resolution and reconstruction accuracy. Hence, the simple triangulation-based 3D PTV method introduced in 1993 (Maas et al. 1993) had limited applications compared to Tomo-PIV for highly seeded flows. Improvements in terms of particle identification (Cardwell et al. 2011) and tracking algorithms (Takehara et al. 2000; Riethmuller 2001; Cowen et al. 1997; Lei et al. 2012; Fuchs et al. 2016, 2017) have been proposed to minimize the error in the measurement.

Recent advancements in terms of reconstruction algorithms, such as Iterative Particle Reconstruction (IPR) (Wieneke 2013) and shake-the-box (STB) (Schanz et al. 2016) have significantly improved the accuracy of 3D PTV. IPR uses an initial triangulation-based reconstructed field to construct a projected image and then minimizes the intensity residuals in the image plane by the "shaking" operation, which shifts the 3D particle position by ± 0.1 voxels in the world coordinate location. This process achieves a better positional accuracy and a reduced fraction of "ghost" particles, which are falsely reconstructed due to ambiguities in matching during triangulation process. The IPR reconstruction accuracy is comparable to intensity-based Multiplicative Algebraic Reconstruction Technique (MART) (Elsinga et al. 2006), for up to a seeding density of 0.05 particles per pixels (ppp). This concept has been further advanced in STB, which uses the temporal information, for a timeresolved measurement, to predict the particle location in the future frames and correct the predicted position iteratively using IPR. Such measurements have successfully resolved flow structures for experiments with high particle concentrations (up to 0.125 ppp). With such capabilities, 3D PTV measurements have gained renewed attention and applicability in various experiments.

To analyze any experimental results with statistical significance, uncertainty quantification is crucial, especially, where the measured data are used in a design process or to validate computational models (Angioletti et al. 2005; Ferreira et al. 2007; Ford et al. 2008; van Ooij et al. 2012; Brindise et al. 2019). Given the increasing applicability and relevance of PTV/IPR/STB volumetric measurements, providing uncertainty estimation for an individual 3D PTV measurement is now of paramount importance.

Uncertainty estimation in PIV measurements has received interest only recently and several methods have been proposed for planar PIV uncertainty quantification. Broadly, such methods can be categorized into direct and indirect methods. Indirect methods rely on a calibration function, which maps an estimated measurement metric (e.g., correlation-plane



signal-to-noise ratio metrics (Charonko and Vlachos 2013; Xue et al. 2014, 2015) or estimates of the fundamental sources of error (Timmins et al. 2012) to the desired uncertainty values. Such a calibration is developed from a simulated image database and may not be sensitive to a specific error source for a given experiment. Direct methods, on the other hand, rely directly on the measured displacements and use the image plane "disparity" (Sciacchitano et al. 2013; Wieneke 2015) information or correlation-plane PDF (probability density function) of displacement information (Bhattacharya et al. 2018) to estimate the a-posterior uncertainty values. Comparative assessments (Sciacchitano et al. 2015; Boomsma et al. 2016) have shown that the direct methods are more sensitive to the random error sources. However, indirect methods can be potentially used to predict any bias uncertainty. A direct uncertainty estimation for stereo-PIV measurement (Bhattacharya et al. 2017) has also been proposed recently. A detailed review of such methods can be found in (Sciacchitano 2019). Thus, although the foundations have been laid for planar and stereo-PIV uncertainty quantification, applicability of such methods to 3D measurements remains untested and these methods train strictly to cross-correlation-based measurements. As a result, 3D reconstruction and tracking process for 3D PTV measurements is not covered under these methods and, currently, a posterior uncertainty quantification methods for volumetric measurements (PTV/PIV) do not exist and new uncertainty model development is needed.

A flowchart for the different steps in a 3D PTV measurement chain is shown in Fig. 1. The first step establishes a mapping function between the camera c image coordinates $\vec{X}^c = \{X^c Y^c\}$ and the world coordinates $\vec{x}_w = \{x_w y_w z_w\}$ in the physical space using a multi-camera calibration process. The calibration coefficients \vec{a}^c are then iteratively corrected using the mapping function and the recorded particle images to eliminate any misalignment between the assumed world coordinate system origin of the calibration plane and the actual origin location for the measurement volume. This process is called volumetric self-calibration (Wieneke 2008) and is essential in minimizing the reconstruction error (due to existing offset or disparity between cameras) and improving the calibration accuracy. Using the modified calibration, for each particle in a given camera, the corresponding match in the second camera is searched along the epipolar line and the particle matches in all cameras are triangulated (Maas et al. 1993; Wieneke 2008) to a 3D world position. This reconstruction process can be done in an iterative sense for an IPR-type algorithm. However, for the particle-pairing process in each camera view, the matching ambiguity

increases for higher particle concentrations, which leads to erroneous reconstructions and is considered one of the main sources of error in the process. Finally, the reconstructed 3D particle positions are tracked to find the velocity vectors using "nearest neighbor" (Malik et al. 1993) or other advanced algorithms (Okamoto et al. 1995; Guezennec et al. 1994; Li et al. 2008; Mikheev and Zubtsov 2008; Fuchs et al. 2017; Cierpka et al. 2013; Cardwell et al. 2011). The tracking and reconstruction can be done in conjunction for STB-type evaluations. From calibration fitting error, particle position estimation error, the disparity vector estimation error to the error in finding the 3D positions, and its pairing, the errors in each step of the process are inter-linked in a complex non-linear way and affect the overall error propagation. The iterative corrections and the governing non-linear functions lead to several interdependent error sources making the definition of a data reduction equation intractable and the development of an uncertainty quantification model non-trivial.

In the current framework, a model is developed to quantify the uncertainty in particle image position and the mapping function coefficient. These uncertainties are in turn combined with the uncertainty propagation through the reconstruction process. Finally, the uncertainty in the velocity vector is expressed directly as a combination of the position uncertainty in the matching pair of particles. The methodology is described in detail in the next section.

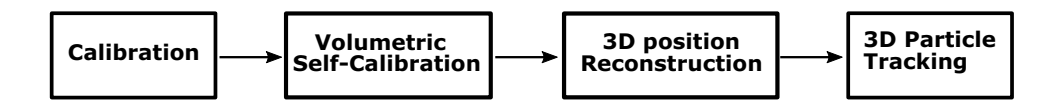
2 Methodology

The primary relation between the observed image coordinates $\vec{X}^c = \{X^cY^c\}$ and the expected particle world coordinates $\vec{x}_w = \{x_w y_w z_w\}$ in physical space is expressed using the individual camera mapping function F_{X^c} for each camera c, as given by:

$$\begin{split} X^c &= F_{X^c} \left(x_w, y_w, z_w, \vec{a}^c \right) = & a_1^c + a_2^c x_w + a_3^c y_w + a_4^c z_w \\ &\quad + a_5^c x_w^2 + a_6^c x_w y_w + a_7^c y_w^2 + a_8^c x_w z_w \\ &\quad + a_9^c y_w z_w + a_{10}^c z_w^2 + a_{11}^c x_w^3 + a_{12}^c x_w^2 y_w \\ &\quad + a_{13}^c x_w y_w^2 + a_{14}^c y_w^3 + a_{15}^c x_w^2 z_w + a_{16}^c x_w y_w z_w \\ &\quad + a_{17}^c y_w^2 z_w + a_{18}^c x_w z_w^2 + a_{19}^c y_w z_w^2 \end{split}$$

A similar functional relationship exists for Y^c , given by $Y^c = F_{Y^c}(x_w, y_w, z_w, \vec{a}^c)$. The vector $\vec{a}^c = \{a_i^c\}$ represents a set of mapping function coefficients for each camera. Typically, a polynomial mapping function is used following Soloff et al. (1997) to have higher accuracies in the presence

Fig. 1 A volumetric PTV measurement chain showing the main steps in the process





of optical distortion effects. Once a mapping function is established and iteratively corrected using a self-calibration process, the reconstruction process involves finding an inverse of the mapping function for the matching particle image coordinates in different projections. Hence, an error propagation through the mapping function is the starting point of the uncertainty quantification and is described in the next subsection.

2.1 Error propagation through the mapping function

An error propagation for Eq. (1) can be written as:

$$e_{X^{c}} = \frac{\partial F_{X^{c}}}{\partial x_{w}} e_{x_{w}} + \frac{\partial F_{X^{c}}}{\partial y_{w}} e_{y_{w}} + \frac{\partial F_{X^{c}}}{\partial z_{w}} e_{z_{w}} + \sum_{i=1}^{19} \frac{\partial F_{X^{c}}}{\partial a_{i}^{c}} e_{a_{i}^{c}}$$
(2)

Equation (2) is obtained as a Taylor series expansion of Eq. (1), neglecting the higher order terms. Thus, the error in image coordinate e_{X^c} can be related to the error in world coordinate positions e_{x_w} , e_{y_w} , e_{z_w} and the error in calibration function coefficients $e_{a_c^c}$ through the mapping function gradients $\left(\frac{\partial F_{X^c}}{\partial x_w}, \frac{\partial F_{X^c}}{\partial z_w}, \frac{\partial F_{X^c}}{\partial z_w}, \frac{\partial F_{X^c}}{\partial a_i^c}\right)$. A similar propagation equation can be written for the error in $Y^c(e_{Y^c})$ image coordinate for each camera mapping function. It is important to note that the quantities of interest are e_{x_w} , e_{y_w} , and e_{z_w} as we seek to estimate the unknown variance in the reconstructed world coordinate positions. Rearranging the unknown terms in the left-hand side, expressing the sums as vector inner products and multiplying each side by its transpose yields the variance propagation equation as follows:

$$\left\{ \frac{\partial F_{X^{c}}}{\partial x_{w}} \frac{\partial F_{X^{c}}}{\partial y_{w}} \frac{\partial F_{X^{c}}}{\partial z_{w}} \right\} \left\{ e_{x_{w}} e_{y_{w}} e_{z_{w}} \right\}^{T} \\
\times \left(\left\{ \frac{\partial F_{X^{c}}}{\partial x_{w}} \frac{\partial F_{X^{c}}}{\partial y_{w}} \frac{\partial F_{X^{c}}}{\partial z_{w}} \right\} \left\{ e_{x_{w}} e_{y_{w}} e_{z_{w}} \right\}^{T} \right)^{T} \\
= \left(e_{X^{c}} - \left\{ \frac{\partial F_{X^{c}}}{\partial a_{i}^{c}} \right\}_{1 \times 19} \left\{ e_{a_{i}^{c}} \right\}_{19 \times 1}^{T} \right) \\
\times \left(e_{X^{c}} - \left\{ \frac{\partial F_{X^{c}}}{\partial a_{i}^{c}} \right\}_{1 \times 19} \left\{ e_{a_{i}^{c}} \right\}_{19 \times 1}^{T} \right)^{T}$$
(3)

The error in particle image position estimation (e_{X^c}) is a function of particle image fitting error and can be assumed to be independent of the error in calibration function coefficients $(e_{a_i^c})$. However, the calibration error can influence the error in projected particle image location or the projection error and, thus, any covariance between e_{X^c} and $e_{a_i^c}$ is implicitly accounted in the projection error formulation, as discussed in Sect. 2.2. With these considerations, a simplified version of Eq. (3) can be written as:

$$\left\{ \frac{\partial F_{X^{c}}}{\partial x_{w}} \frac{\partial F_{X^{c}}}{\partial y_{w}} \frac{\partial F_{X^{c}}}{\partial z_{w}} \right\} = \sum_{\vec{x}_{w}} \left\{ \frac{\partial F_{X^{c}}}{\partial x_{w}} \frac{\partial F_{X^{c}}}{\partial y_{w}} \frac{\partial F_{X^{c}}}{\partial z_{w}} \right\}^{T}$$

$$= \sigma_{X^{c}}^{2} + \left\{ \frac{\partial F_{X^{c}}}{\partial a_{i}^{c}} \right\} = \sum_{\vec{a}^{c}} \left\{ \frac{\partial F_{X^{c}}}{\partial a_{i}^{c}} \right\}^{T}$$
(4)

Here, $\left\{ \frac{\partial F_{X^c}}{\partial x_w} \frac{\partial F_{X^c}}{\partial y_w} \frac{\partial F_{X^c}}{\partial z_w} \right\}$ is a row vector containing mapping function gradients for each camera c with respect to $\vec{x}_w = \{x_w y_w z_w\}$ and $\overline{\Sigma}_r$ represents the unknown covariance matrix in world coordinates ($\overline{\Sigma}_{\vec{x}_w} = \left\{ e_{x_w} e_{y_w} e_{z_w} \right\}^t \left\{ e_{x_w} e_{y_w} e_{z_w} \right\}$). The uncertainty in particle image position X^c is denoted by σ_{X^c} . The term $\left\{\frac{\partial F_{X^c}}{\partial a_c^c}\right\} \overline{\sum}_{\vec{a}^c}^{-c} \left\{\frac{\partial F_{X^c}}{\partial a_c^c}\right\}^T$ evaluates to a single numerical value, which accounts for the contribution from the uncertainty in the calibration coefficients $\vec{a}^c = \{a_i^c\}_{1 \times 19}$, for the mapping function F_{X^c} of camera c. The vector $\left\{\frac{\partial F_{X^c}}{\partial a^c_i}\right\}_{1 \times 19}$ represents the mapping function gradients with respect to the calibration coefficients \vec{a}^c and the covariance in mapping function coefficients for each camera is denoted by $\sum_{\vec{a}^c}^c = \left\{ e_{a_i^c} \right\}_{19 \times 1}^T \left\{ e_{a_i^c} \right\}_{1 \times 19}^T$ Now, Eq. (4) is written only for camera c mapping function $F_{X^{c}}$. To solve for $\overline{\Sigma}_{\vec{x}}$, Eq. (4) is stacked up for all N cameras and for both F_{Y^c} and F_{Y^c} mapping functions, which leads to 2 N number of rows in the final matrix form of the equation. For example, for a four-camera set-up, the combined equation for all cameras will have 8 rows and is expressed as:

Each term in Eq. (5) has the dimension $2N \times 2N$ and the $\overline{\overline{\overline{z}}}_{\vec{x}_{...}}$ term is solved for each reconstructed particle individually. In Eq. (5), $\overline{C}_{\vec{x}_w}$ is a $2N \times 3$ coefficient matrix containing mapping function gradients for the 2N mapping functions. The combined variance matrix in particle image position \overline{X}^c is denoted by $\overline{\Sigma}_{\overline{X}^c}$ and contains $\sigma^2_{X^c}$ and $\sigma^2_{Y^c}$ as diagonal entries for each camera. The correlation between e_{X^c} and e_{Y^c} is assumed to be negligible. Also, the correlation of e_{X^c} , e_{Y^c} between different camera components is neglected as the σ_{X^c} , σ_{Y^c} estimates are obtained independently for each camera. Hence, the off-diagonal terms of $\Sigma_{\vec{y}^c}$ are set to zero. Finally, the evaluated scalar values of $\left\{ \frac{\partial F_{X^c}}{\partial a_i^c} \right\} \overline{\overline{\Sigma}}_{\vec{a}^c}^c \left\{ \frac{\partial F_{X^c}}{\partial a_i^c} \right\}^T \text{ for each mapping function in Eq. (4)}$ are put as the diagonal terms in the $\overline{\Sigma}_{a}^{c}$ matrix, which represents the net calibration uncertainty contribution across all N cameras. Thus, Eq. (5) contains the unknown covariance matrix in world coordinates $\overline{\Sigma}_{\vec{x}_{o}}$ as a function of $\overline{\Sigma}_{\vec{v}}$ and $\overline{\Sigma}_{\vec{a}}$. The following sections focus on estimating the $\overline{\Sigma}_{\vec{v}}$ and $\overline{\Sigma}_{\vec{a}^c}$ terms.



The overview of the uncertainty estimation and propagation process is depicted in Fig. 2.

2.2 Estimating uncertainty in particle image location

For a-posteriori uncertainty quantification, we start from the reconstructed 3D particle positions obtained either from a triangulation or IPR reconstruction method. For a given 3D particle position, we want to find the corresponding

projected particle image locations and its uncertainty for each camera. As shown in Fig. 2a, the projected particle image positions are compared with the recorded image to find the error in particle image location. This can be expressed as a sum of the estimated projection error $(\vec{X}^c - \vec{X}^c_{est})$ and the 2D particle fit position estimation error $(\vec{X}^c - \vec{X}^c_{est})$ for all \vec{X}^c and for each camera c, as shown in the following equation:

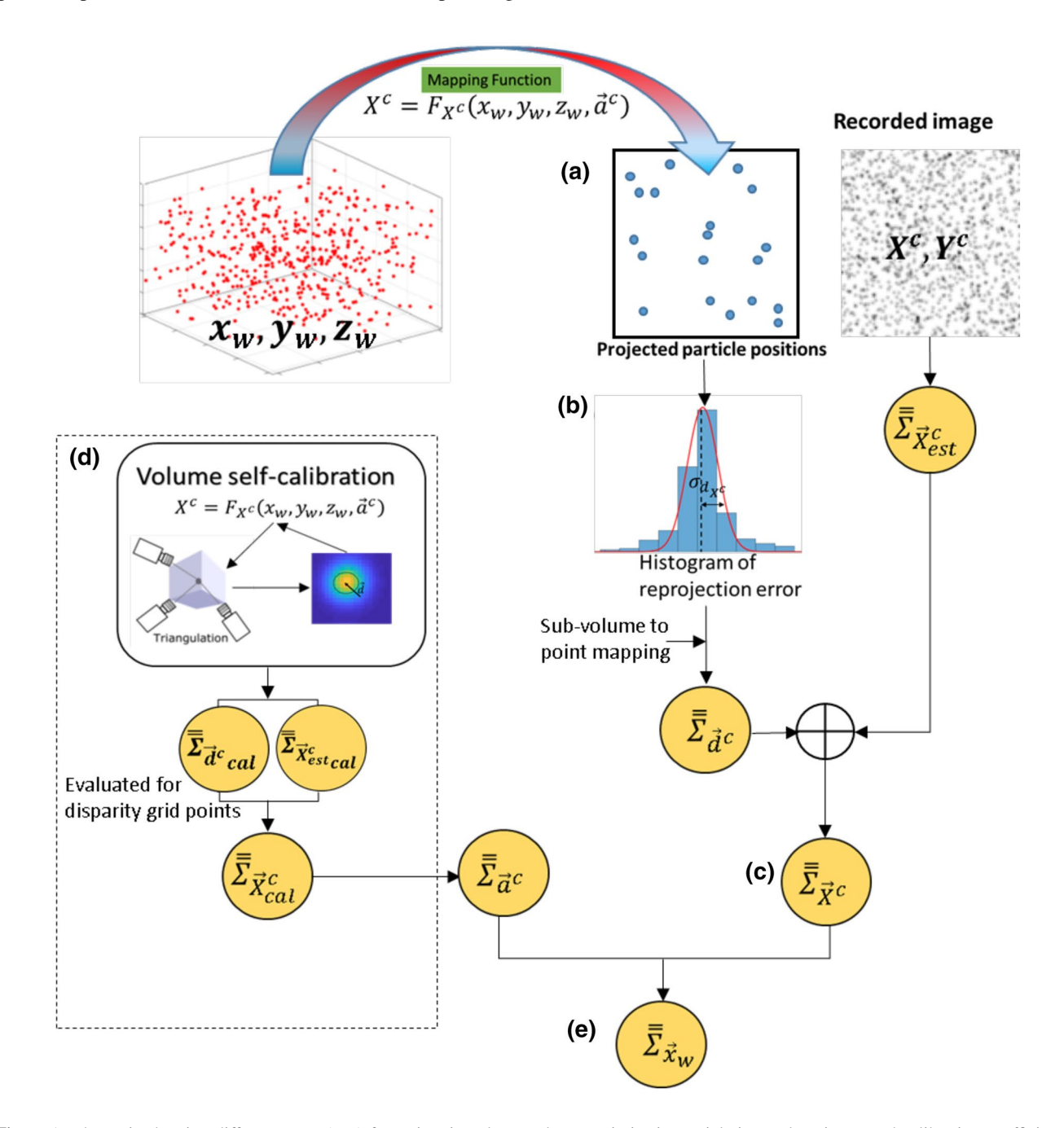


Fig. 2 A schematic showing different steps $(\mathbf{a}-\mathbf{e})$ for estimating elemental uncertainties in particle image location X and calibration coefficients a_i and its propagation to the uncertainty in the world coordinate x_w



$$e_{\overrightarrow{X}^c} = \overrightarrow{X}^c - \overrightarrow{X}_{true}^c = \overrightarrow{X}^c - \overrightarrow{X}_{est}^c + \overrightarrow{X}_{est}^c - \overrightarrow{X}_{true}^c$$
 (6)

Thus, the variance in particle image location, $\overline{\Sigma}_{\overrightarrow{X}}$, becomes a sum of the variance in the estimated projection error, denoted by $\overline{\overline{\Sigma}}_{\overrightarrow{d}}$, and the variance of the error in particle image position estimation $(\overline{\Sigma}_{\overrightarrow{V}}^c)$, as given by:

$$\overline{\Sigma}_{\overrightarrow{X}^c} = \overline{\Sigma}_{\overrightarrow{d}^c} + \overline{\Sigma}_{\overrightarrow{X}_{est}^c}$$
(7)

As mentioned in Sect. 2.1 Eq. (5), each of these variance matrices is diagonal matrices with dimension 2 N × 2 N. The $\overline{\Sigma}_{\overline{X}^c}$ matrix has the diagonal entries $\sigma_{X^c}^2$ and $\sigma_{Y^c}^2$ corresponding to X^c and Y^c image coordinates for each of the N cameras. To estimate $\overline{\Sigma}_{i}$, the reconstruction domain is divided into sub-volumes and the estimated projection error for a group of particles belonging to the same sub-volume is stacked up into a histogram. This is similar to the concept of disparity $(\vec{d} = \{d_{X^c}d_{Y^c}\})$ for each camera c as defined by Wieneke (2008). The sub-volume size can be varied or particles from other frames can be included to have a larger statistical sample. Simulations using synthetic images showed that a histogram consisting of 50 or more particles in the sub-volume yields a statistically consistent estimate, irrespective of the number of sub-volumes considered. Such a histogram of disparity (\vec{d}) estimates is shown in Fig. 2b, where the standard deviation in the estimated X^c projection error is denoted by $\sigma_{d_{vc}}$. For a perfectly converged self-calibration, the mean disparity $(\vec{d}^{\,c})$ should be zero. Typically, the disparity histogram approaches a Gaussian distribution and, for the robustness of variance estimation, a Gaussian fit is applied on this histogram. The estimated standard deviation from the fitted curve is used to evaluate the variance of the disparity distribution. However, for a lower seeding density, the disparity distribution is observed to deviate from a Gaussian distribution. Consequently, if the area under the fitted Gaussian curve is different by more than 5% compared to the histogram area evaluated using trapezoidal integration rule, the standard deviation of the distribution is used as the standard uncertainty. In this framework, this estimated variance is modeled as the desired $\overline{\Sigma}_{d}^{c}$ of Eq. (7). For the particles belonging to the same sub-volume, the same value of $\overline{\Sigma}_{\vec{\tau}^c}$ is

The $\overline{\Sigma}_{\overrightarrow{X}_{est}}^c$ term in Eq. (7) consists of the $\sigma_{X_{est}^c}^2$ and $\sigma_{Y_{est}^c}^2$ terms as diagonal entries for each camera. To estimate these variance terms, each particle image within ± 0.5 pixels of the projected 3D particle location is fitted with a Gaussian shape and, thus, the uncertainty in the fitted position parameter for the least-square fit process is considered. Thus, the $\sigma_{X_{est}^c}^2$ term is given by:

$$\sigma_{X_{est}^{c}}^{2} = diag\left(\left(\overline{\overline{J}}^{T}\overline{\overline{J}}\right)^{-1}\right)\sigma_{res}^{2} \tag{8}$$

Equation (8) denotes an expression for the X_{est}^c position estimation variance which is shown to be a function of the variance in the fit residual error (σ_{res}^2) and the Jacobian (\overline{J}) of the residual at the solution point. A similar expression can be written for $\sigma_{Y_{est}^c}^2$ term. Here, the \overline{J} matrix consists of the gradient of the objective function for the minimization process with respect to the estimated parameters (X_{est}^c) or Y_{est}^c for the Gauss-

ian least-square fit. The matrix $\left(\overline{J}^T\overline{J}\right)^{-1}$ has the dimension $N_{param} \times N_{param}$, where N_{param} denotes the number of parameters estimated in the least-squares solver. Hence, in Eq. (8), the i^{th} diagonal is considered to estimate the variance in the i^{th} parameter. This estimation is consistent with the Cramer–Rao lower bound (CRLB) determination for 2D particle image centroid, as highlighted by (Rajendran 2019). Hence, once $\overline{\Sigma}_{ac}$ and $\overline{\Sigma}_{X_{est}}$ are estimated, the $\overline{\Sigma}_{X_{est}}$ is known (Fig. 2c).

2.3 Estimating the uncertainty in mapping function coefficients

As seen from the flowchart in Fig. 2, once the variance in particle image position $(\overline{\Sigma}_{\overrightarrow{\mathbf{v}}^c})$ is estimated through the progression of steps shown on the right side, the next workflow is focused on estimating the variance in the calibration coefficients $(\overline{\Sigma}_{\vec{a}^c})$. The overall calibration uncertainty $\overline{\Sigma}_{\vec{a}^c}$ is a combination of $\overline{\Sigma}_{2^c}$ for each camera c. The $\overline{\Sigma}_{2^c}$ estimation process (Fig. 2d) can be performed in conjunction with the volumetric self-calibration process. In the absence of selfcalibration, the uncertainty in the coefficients $\{a_i^c\}$ is dictated by the uncertainty in calibration image dot fitting. However, the presence of disparity between estimated and projected points leads to a shift in the projected calibration grid points $\vec{X}_{cal}^c = \{X_{cal}^c Y_{cal}^c\}$ in the image domain, and this correction leads to a new set of coefficients $\{a_i^c\}$ in the self-calibration process. Hence, the uncertainty in X_{cal}^c , Y_{cal}^c positions, namely $\overline{\overline{\Sigma}}_{\overrightarrow{X}^c}$, should directly affect the $\overline{\Sigma}_{\overrightarrow{a}^c}$. If we consider the world coordinate positions $\vec{x}_{w_{cal}} = \{x_{w_{cal}} y_{w_{cal}} z_{w_{cal}}\}$ where the disparity vectors are evaluated during the volume selfcalibration process, then $\vec{x}_{w_{cal}}$ grid points will have no uncertainty in their location as those points are defined fixed locations in space. Consequently, the unknowns $(e_{x_w}, e_{y_w}, e_{z_w})$ of Eq. (3) for the $\vec{x}_{w_{col}}$ grid points can be simplified to zero and the other terms can be further simplified as shown:



$$\overline{\overline{\Sigma}}_{X_{cal}^c} = \overline{\overline{C}}_{\overline{a}^c} \overline{\overline{\Sigma}}_{\overline{a}^c}^{-C} \overline{\overline{C}}_{\overline{a}^c}^{-T}$$

$$\tag{9}$$

In Eq. (9), the $\overline{\overline{C}_{a^c}}$ represents the matrix of gradients of the mapping function with respect to the coefficients a_i , $\left[\frac{\partial F_{X^c}}{\partial a_i^c}\right]$ or $\left[\frac{\partial F_{Y^c}}{\partial a_i^c}\right]$, having 19 columns and number of rows corresponding to number of calibration or disparity grid points (N_{cal}) . The $\overline{\Sigma}_{a^c}^c = \left\{e_{a_i^c}\right\}_{19\times 1}^T \left\{e_{a_i^c}\right\}_{1\times 19}$ is the unknown covariance matrix for the coefficients \overline{a}^c belonging to either mapping function F_{X^c} or F_{Y^c} of camera c. Thus, Eq. (9) is solved for $\overline{\Sigma}_{\overline{a}^c}^c$ with each set of \overline{a}^c over all the disparity grid points N_{cal} . The variance in the particle image position $\overline{\Sigma}_{\overline{X}_{cal}^c}^c$ is a $N_{cal} \times N_{cal}$ diagonal matrix with $\sigma_{X_{cal}^c}^2$ or $\sigma_{Y_{cal}^c}^2$ terms as diagonal entries, which can be evaluated for the disparity grid points in a similar way as mentioned in Eqs. (7) and (8) of Sect. 2.2. Here, the $\overline{\Sigma}_{\overline{X}_{cal}^c}$ can be evaluated for the initially

triangulated particle positions and is used in Eq. (9) to solve

2.4 Uncertainty propagation in reconstructed positions

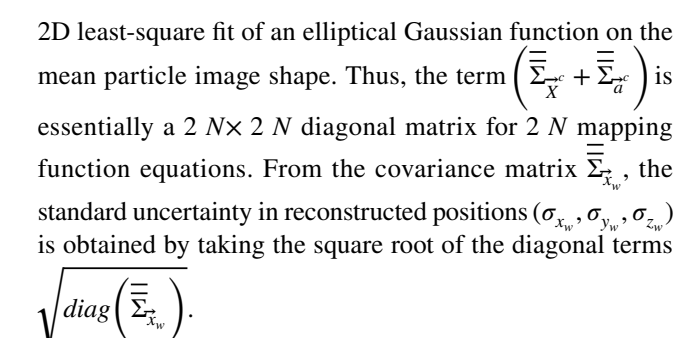
for \sum_{a}^{∞} as a least-squares problem for all N_{cal} .

The uncertainty in the reconstructed world coordinate position is finally obtained by solving for the world coordinate location covariance matrix $\overline{\Sigma}_{\vec{\chi}_w}$ from Eq. (5), as shown in Fig. 2e. This equation is evaluated for each world coordinate position combining mapping functions in X^c and Y^c for all 2 N cameras. The estimated covariance $\overline{\Sigma}_{\vec{a}^c}^c$ term in Sect. 2.3 is used to evaluate the scalar values $\left\{\frac{\partial F_{X^c}}{\partial a_i^c}\right\}\overline{\Sigma}_{\vec{a}^c}^c\left\{\frac{\partial F_{X^c}}{\partial a_i^c}\right\}^T$ or $\left\{\frac{\partial F_{Y^c}}{\partial a_i^c}\right\}\overline{\Sigma}_{\vec{a}^c}^c\left\{\frac{\partial F_{Y^c}}{\partial a_i^c}\right\}^T$, which are used as diagonal entries to compute $\overline{\Sigma}_{\vec{a}^c}$, as mentioned in Eq. (4) of Sect. 2.1. The $\overline{\Sigma}_{\vec{x}^c}^c$ has already been calculated using Eq. (7). Hence, we solve for $\overline{\Sigma}_{\vec{x}_w}$ by inverting the $\overline{C}_{\vec{x}_w}$ matrix as given by the following equation:

$$\overline{\overline{\Sigma}}_{\vec{X}_w} = \overline{\overline{B}} \left(\overline{\overline{\Sigma}}_{\vec{X}}^c + \overline{\overline{\Sigma}}_{\vec{a}}^c \right) \overline{\overline{B}}^{-1}$$
 (10)

Here, $\overline{\overline{B}}$ is given by $\overline{\overline{B}} = \left(\overline{\overline{C}}_{\vec{x}_w}^T \overline{\overline{C}}_{\vec{x}_w}\right)^{-1} \overline{\overline{C}}_{\vec{x}_w}^T$. It can be noted

that for standard Gaussian particle images, the covariance between X^c and Y^c particle image position estimation can be assumed to be negligible. However, in the presence of optical distortion, such a covariance can be estimated from the



We also evaluate the bias uncertainty terms $\sigma_{x_{w_b}}$, $\sigma_{y_{w_b}}$, $\sigma_{z_{w_b}}$, the mean disparity is negligible. However, due to measurement noise, any residual mean disparity (d^c) can lead to a bias in the reconstructed position measurement. We estimate d^c from the disparity histogram and use that to estimate $\overline{\Sigma}_{x_b}^c$, the bias uncertainty in particle image position and $\overline{\Sigma}_{x_b}^c$, the bias uncertainty is \overline{d}^c using the propagation Eqs. (7) and (9). For $\overline{\Sigma}_{x_b}^c$, only $\overline{\Sigma}_{d_b}^c$ is considered in Eq. (7). The final bias uncertainty estimates for reconstructed x_w , y_w , z_w positions are obtained using the propagation Eq. (10) by substituting the values of $\overline{\Sigma}_{x_b}^c$ and $\overline{\Sigma}_{x_b}^c$.

2.5 Uncertainty in estimated velocity field

Once the reconstructed 3D particle positions are obtained, the tracked velocity estimate is a function of the particle-pairing process. For particle displacements higher than the mean inter-particle distance, the particle matching becomes challenging, especially the nearest-neighbor search fails in most cases. This leads to erroneous measurements and significant percentage of outliers. However, here, we only consider the tracked velocity for particles that are successfully paired, defined by particle tracks with error magnitude less than 1 voxels. In such cases, the uncertainty in each tracked 3D velocity measurement is evaluated as a direct combination of the estimated 3D position uncertainties of each paired particle. Thus, if a particle in frame 1 ($\sigma_{x_{w1}}$, $\sigma_{y_{w1}}$, $\sigma_{z_{w1}}$) is paired with a particle in frame 2, then the uncertainty in the tracked displacement σ_u is given by:

$$\sigma_u^2 = \sigma_{x_{w_b}}^2 + \sigma_{x_{w_1}}^2 + \sigma_{x_{w_2}}^2 - \rho_{x_{w_1} x_{w_2}} \sigma_{x_{w_1}} \sigma_{x_{w_2}}$$
 (11)

In Eq. (11), $\sigma_{x_{w_b}}$ is the bias uncertainty term as evaluated in Sect. 2.4. The bias uncertainty depends on the mean disparity and the mapping function coefficients, and is not expected to change from frame to frame. Hence, it is accounted for only once in the tracking uncertainty estimation. For the synthetic test case, we observed that the true position error in the estimated 3D particle position for a



paired particle in frame 1 and frame 2 has a strong correlation. Thus, the covariance term $\rho_{x_{w1}x_{w2}}\sigma_{x_{w1}}\sigma_{x_{w2}}$ in Eq. (11) is significant, and at first, the correlation coefficient $\rho_{x_{w_1}x_{w_2}}$ (for x component) is evaluated. For synthetic test case, with true error fields $e_{\mathbf{x}_{wl}}$ and $e_{\mathbf{x}_{w2}}$, the $\rho_{\mathbf{x}_{wl},\mathbf{x}_{w2}}$ has been observed to vary from about 0.5 to 0.8; however, in general, $\rho_{x_{wl}x_{wl}}$ can assume any value between 0 and 1, depending on the flow field and calibration. Since the 3D particle position error has a significant contribution from the particle reprojection error or disparity error $(\vec{X}^c - \vec{X}_{est}^c)$, the 3D position error correlation between successive frames is expected to have a similar magnitude compared to the disparity error correlation, which is verified for synthetic test cases with known error. In the present case, this $\rho_{x_{w1}x_{w2}}$ is estimated in an average sense using the correlation of the reprojection errors between successive time frames. Here, we first calculate the disparity error for each reconstructed particle and for each camera. The disparity values (\vec{d}) for all particles for a specific camera in frame 1 are then correlated with the disparity values of the matching particles (obtained with 3D tracking) for the same camera in frame 2. Finally, the mean value of the correlation coefficients obtained for each pair of frames and for each camera is used as an estimate for $\rho_{x_{w1},x_{w2}}$. To capture any variation in $\rho_{x_{w1}x_{w2}}$ over the 3D domain and also over the time-series, this term can be computed only for each pair of frames and also for a statistically significant number of reconstructed particles within a sub-volume to avoid any global averaging effects. However, if the spatio-temporal variations of $\rho_{x_{\omega_1},x_{\omega_2}}$ is insignificant, then a global mean estimate of the coefficient may be used to calculate the covariance term. The uncertainty in v and w components (σ_v, σ_w) can be obtained in a similar way following Eq. (11). It is to be noted that the uncertainty due to false matching in the presence of ghost particles may need further analysis. However, for a valid measurement, we expect Eq. (11) to account for the uncertainty in the tracked velocity measurement.

The current framework estimates the uncertainty in a 3D PTV measurement for dual-frame tracking. However, for time-resolved measurements the 3D trajectory is usually fit with a second-order polynomial or B-spline or a Wiener filter over several particle positions in successive frames to increase the trajectory accuracy, as discussed in recent articles by (Cierpka et al. 2013), (Schanz et al. 2016) and (Van Gent et al. 2017). For such analysis, the current methodology can be extended to include multiframe trajectory fitting uncertainty by combining the estimated uncertainty in the reconstructed position with the uncertainty in the fitting coefficients. For example, with polynomial fitting, if $x_{wfit} = p_0 + p_1 x_w + p_2 x_w^2$ is the second-order fit equation, then the uncertainty in the fitted x_w posi-

tion can be expressed as
$$\sigma_{x_{wfit}}^2 = diag \left(\overline{\overline{J}}_{fit} \left(\overline{\overline{J}}_{fit}^T \overline{\overline{\Sigma}}_{x_w}^{-1} \overline{\overline{J}}_{fit} \right)^{-1} \overline{\overline{J}}_{fit}^T \right)$$

(Gavin 2011). Here, $\left[\overline{J}_{fit}\right]_{ij} = \frac{\partial x_{wi}}{\partial p_j}$ is the Jacobian, representing the gradient of the ith temporal position x_{wi} of a single particle track with respect to the coefficient p_j . The $\left[\overline{\overline{\Sigma}}_{x_w}\right]_{ij} = \left(\rho_{x_{wi}x_{wj}}\sigma_{x_{wi}}\sigma_{x_{wj}}\right)^2$ is the covariance matrix of the reconstructed x_w positions in successive frames. The current framework gives an estimate of $\rho_{x_{wi}x_{wj}}$ and $\sigma_{x_{wi}}$, $\sigma_{x_{wj}}$ terms which can be used to directly compute the uncertainty $\sigma_{x_{wjt}}^2$ in the fitted trajectory. Uncertainty in advanced models for fitting a particle trajectory and its performance with varying noise and particle concentration can be explored in a future analysis.

3 Results

The proposed framework to estimate the uncertainty in the reconstructed particle positions is tested using synthetic vortex ring images. The particle field was generated and advected using incompressible axisymmetric vortex ring equations mentioned in Wu et al. (2006). The camera calibration and particle images (256×256 pixels) were generated using in-house code. The camera angles were selected as 35° and the four cameras were positioned in a plus (+) configuration. The volume of interest was set to $42 \text{ mm} \times 42 \text{ mm} \times 24 \text{ mm}$ and the seeding density was varied from 0.01 ppp to 0.1 ppp. The processing was also done using in-house calibration and IPR code for 100 image pairs. A polynomial model was used for the camera calibration and the initial estimate of the calibration was modified by three iterations of volumetric self-calibration to eliminate any mean disparity. An allowable triangulation error of one pixel was used for the initial triangulation with particle identification using dynamic particle segmentation method (Cardwell et al. 2011) to better resolve overlapping particle images. The particle image positions were estimated using least-square Gaussian fit. The optical transfer function (OTF) (Schanz et al. 2013) was calculated and used in IPR iterations. The number of inner loop and outer loop iterations for each frame was set to 4 with particle "shaking" of ± 0.1 voxels. The 3D particle tracking was done using "nearest neighbor" algorithm. The uncertainty for each measurement was computed using the set of equations described in Sect. 2.

3.1 Comparing error and uncertainty histogram for reconstructed particle positions

First, the uncertainty in reconstructed particle positions is analyzed. The reconstructed particle positions are compared with the true particle positions in space, and if a particle is



197 Page 10 of 18 Experiments in Fluids (2020) 61:197

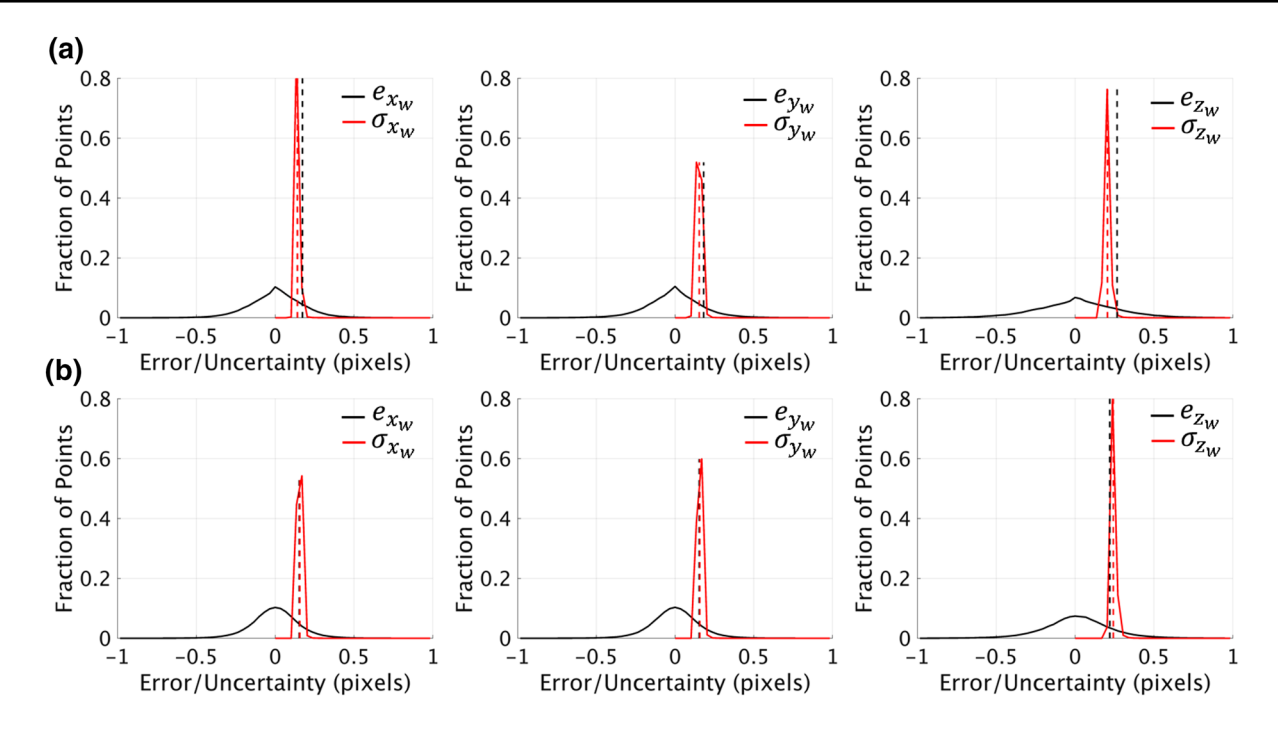


Fig. 3 Histogram of error (*e*) and uncertainty (σ) distributions for reconstructed particle positions (x_w , y_w , z_w) for the synthetic vortex ring case with 0.05 ppp particle concentration for **a** triangulation and

 ${\bf b}$ IPR reconstructions. The vertical lines indicate the RMS value for each distribution

found within 1 voxel radius of the true particle, then it is considered as a valid reconstruction. The error in reconstructed x_w position is denoted by e_x and defined as:

$$e_{x_w} = x_{west} - x_{wtrue} \tag{12}$$

Similarly, e_{y_w} and e_{z_w} are defined. Figure 3 shows the histogram of error and uncertainty distributions x_w , y_w , and z_w coordinates. Figure 3a, b shows the distributions for the reconstructed particle positions obtained using triangulation and IPR methods, respectively, for a particle concentration of 0.05 ppp. The x-axis is divided into 60 equally spaced bins and the y-axis denotes the number of measurements falling within each bin as a fraction of total number of points. The root-mean-squared (RMS) error is defined as:

$$RMS\ error = \sqrt{\frac{1}{N} \sum_{i=1}^{N} e_i^2}$$
 (13)

The error distribution for the triangulated particle positions is wider with RMS error of about 0.17, 0.18, and 0.27 pixels in x_w , y_w , and z_w positions compared to RMS error of 0.15, 0.15, and 0.22 pixels for the IPR case. For the triangulation case, the error distribution is sharp near the zero value and has a longer tail, which can be related to more accurate predictions for isolated particle images and a faster drop in

accuracy for overlapping particle images. For IPR, however, the error distribution looks more Gaussian, which can be attributed to the iterative correction process. The predicted uncertainty distributions have significantly less spread and have a tight distribution around the RMS error. For a successful prediction, it is expected that the RMS value of the error distribution should match the RMS value of the estimated uncertainty distribution (Sciacchitano et al. 2015), assuming that the bias error is negligible. In the synthetic case, the bias error varies in the range of 0.001–0.015 pixels, which is an order of magnitude less than the corresponding RMS error range of 0.09-0.4 pixels. The RMS value for each distribution is indicated by the dashed vertical line. For Fig. 3a, the RMS uncertainty values underpredict the RMS error by 0.03 pixels in x_w and y_w and by 0.06 pixels in z_w . For IPR case in Fig. 3b, the predicted uncertainties are within 0.02 pixels of the RMS error values. The contribution from two main components $\overline{\Sigma}_{\overrightarrow{x}^c}$ and $\overline{\Sigma}_{\overrightarrow{a}^c}$ to the overall uncertainty $\overline{\Sigma}_{\vec{x}}$ is computed using Eq. (10). The calibration uncertainty term $(\Sigma_{\vec{a}})$ is distributed in the lower uncertainty bins and contributes on average to 10% of the combined uncertainty estimate, whereas the particle image position uncertainty has 90% contribution. Overall, the predicted uncertainties are in close agreement with the expected value, indicating a successful prediction for position reconstruction uncertainty.



3.2 Reconstructed position uncertainty for varying particle concentration

The increase in particle concentration leads to a higher percentage of overlapping particle images which increases the error in particle identification and, subsequently, in 3D particle reconstruction. To test the sensitivity of the uncertainty predictions in such scenarios, the seeding density is varied from 0.01 ppp to 0.1 ppp, and the RMS error and uncertainty values are compared in each case, as shown in Fig. 4a, b. The results show a high sensitivity of the predicted uncertainty to the trend of the RMS error for both triangulation and IPR methods. The reconstructed position RMS error predicted by IPR is lesser than the triangulation error for lower seeding densities, whereas, for 0.1 ppp, the IPR error is higher, which may be related to the specifics of the in-house IPR implementation. However, the objective is to predict the correct RMS error level

given the different reconstructed positions using different methodologies. For triangulation, the RMS uncertainty follows the RMS error trend consistently, but underpredicts the magnitude by about 0.04 pixels (23%) at 0.01 ppp and by 0.07 pixels (20%) at 0.1 ppp. For the IPR case, the predicted uncertainty matches the expected uncertainty value closely at 0.01 ppp and 0.05 ppp with a deviation of about 0.01 pixels (10%), but underpredicts the uncertainty by 0.08 pixels (30%) at 0.1 ppp. Overall, the increasing trend agreement, between the predicted and the expected uncertainty validates the current framework for prediction of uncertainty for a wide range of particle concentrations and using both reconstruction methods.

For a more specific comparison across seeding densities, the values of RMS errors and uncertainties in x_w , y_w , and z_w positions for both methods are presented in Fig. 5. The maximum underprediction of about 0.06 pixels occurs at 0.1 ppp case for both methods. The best agreement is obtained

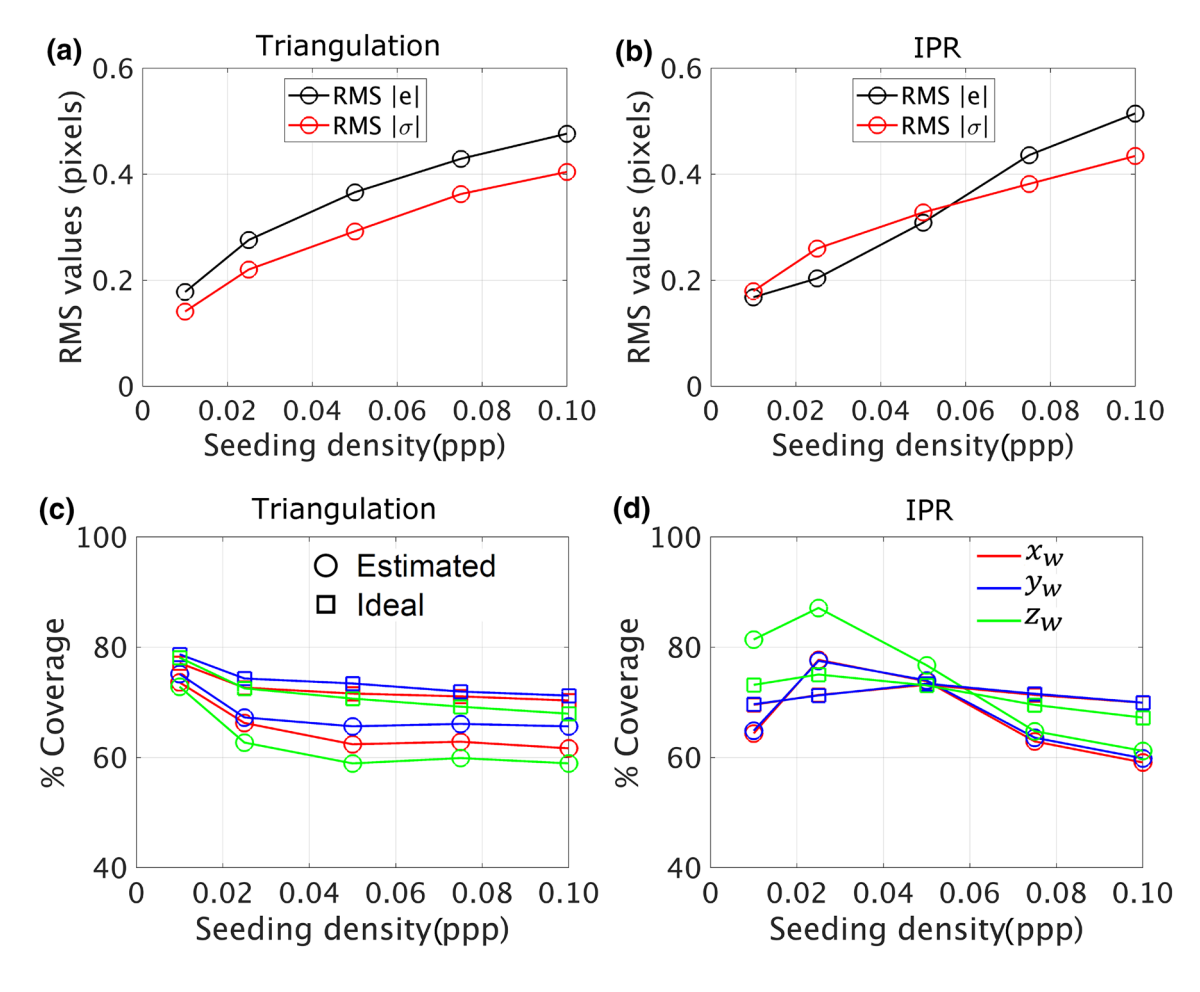


Fig. 4 The RMS of reconstructed position error magnitude (|e|) is compared against the RMS of uncertainty magnitude ($|\sigma|$) in subplots (a and b). The percentage of measurements within the uncertainty bounds (estimated coverage) is compared against percentage of meas-

urements falling within RMS error bounds (ideal coverage) in subplots (\mathbf{c} and \mathbf{d}). The comparison is presented as a function of seeding density in the range of 0.01–0.1 ppp and for triangulation and IPR-based reconstructions



197 Page 12 of 18 Experiments in Fluids (2020) 61:197

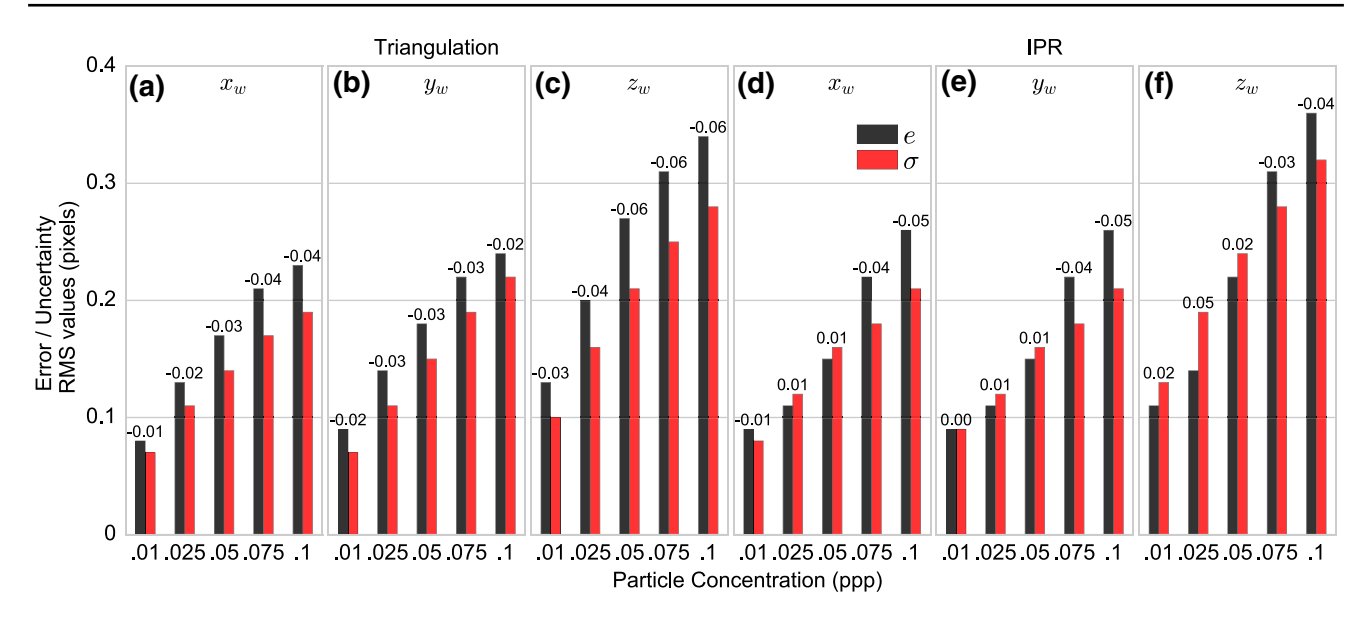


Fig. 5 Comparison of RMS error and RMS uncertainty values for the triangulation- and IPR-based reconstructed particle positions for a range of seeding densities. The difference between the RMS values is mentioned at the top of each grouped bar

for the IPR case for up to 0.05 ppp and for the triangulation case upto 0.025 ppp. It is to be noted that the IPR reconstruction error is higher than exepected, which may be related to a lower convergence rate and, in turn, depends on the specifics of the implementation; however, given a reconstructed field, the current method reasonably predicts the standard uncertainty in 3D particle-based reconstruction.

To compare the global prediction of uncertainty level for all particles, the estimated coverage is plotted in Fig. 4c, d. The coverage (Coleman and Steele 2009) is defined as the percentage of measurement errors falling within the uncertainty bound $(\pm \sigma)$. For an ideal Gaussian error distribution, the standard uncertainty coverage is 68.3%. However, since the error distributions deviate from the Gaussian shape, the estimated coverage is compared with an ideal coverage, which denotes percentage of measurement errors falling within the RMS error bound. In Fig. 4c, the coverage for all cases lies within 60% and 68%, except for 0.01 ppp case for which the coverage is about 74%. For triangulation, the ideal coverage lies in the range of 67–78%. The predicted coverage deviates from the ideal coverage by about 9% to 13%, with a minimum error of 5% for 0.01 ppp case. For IPR, the estimated coverage varies from 60 to 87%, with maximum overprediction for the 0.025 ppp case (16% for z_w , 9% for x_w and y_w) and underprediction (7–15%) for the 0.075 and 0.1 ppp cases, as shown in Fig. 4d. The ideal coverage is in the 69–75% range and best matches the estimated coverage for 0.05 ppp. Any bias in the error distribution can affect the accuracy in coverage prediction. Thus, in the present analysis, the estimated uncertainty coverage metric is mostly in the range of 60-87% and agrees within 16% of the ideal coverage values.

3.3 Uncertainty prediction for tracked velocity vectors

As a final step, the uncertainty prediction in the tracked velocity field is assessed. The reconstructed 3D particle positions are tracked for 100 pairs of frames using nearest-neighbor tracking. The true particle positions in 1 voxel vicinity of the reconstructed particle positions is found for the first frame and the corresponding true displacement is subtracted from the estimated displacement to compute the error (e) in u, v, and w velocity components. A measurement is considered valid if the computed error magnitude is within 1 voxel. The uncertainty (σ_u , σ_v , σ_w) in the velocity components are computed using Eq. (11).

The RMS uncertainty values mentioned in Fig. 6 are in close agreement with the RMS error values with a maximum deviation of 0.04 pixels across all cases. The RMS error increases with the particle concentration due to higher probability of erroneous matches resulting from ghost particle reconstruction. The predicted uncertainty increases proportionally with RMS error, for both reconstruction methods, as observed in Fig. 6.

The histogram of velocity error and uncertainty distribution is compared in Fig. 7a for the triangulation case and Fig. 7b for the IPR case, for 0.05 ppp seeding density. The error distribution is sharper for the triangulation case. It is noticed that the w component has higher error compared to u and v components. For all cases, the uncertainty distributions have a very narrow spread and predicts the RMS error magnitude perfectly. Further analysis is required to validate



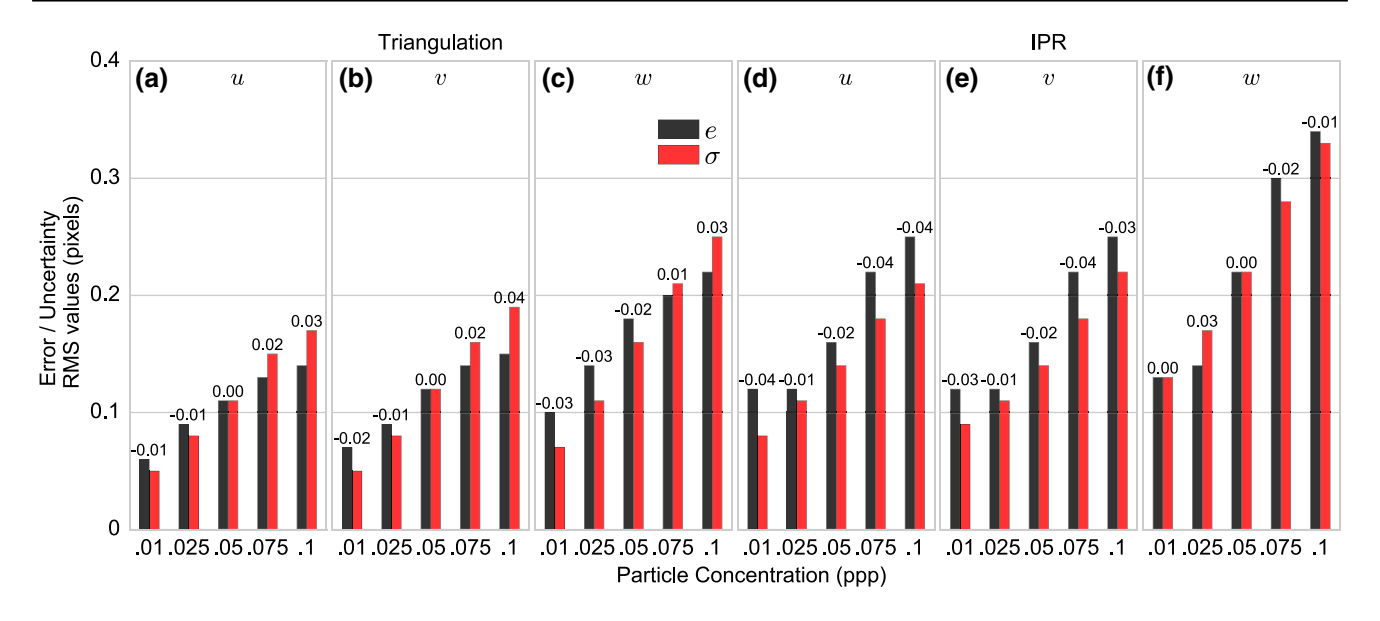


Fig. 6 Comparison of RMS error and RMS uncertainty values for the particle tracking displacement estimates using triangulation and IPR-based reconstructed particle positions for a range of seeding densities.

The difference between the RMS values is mentioned at the top of each grouped bar

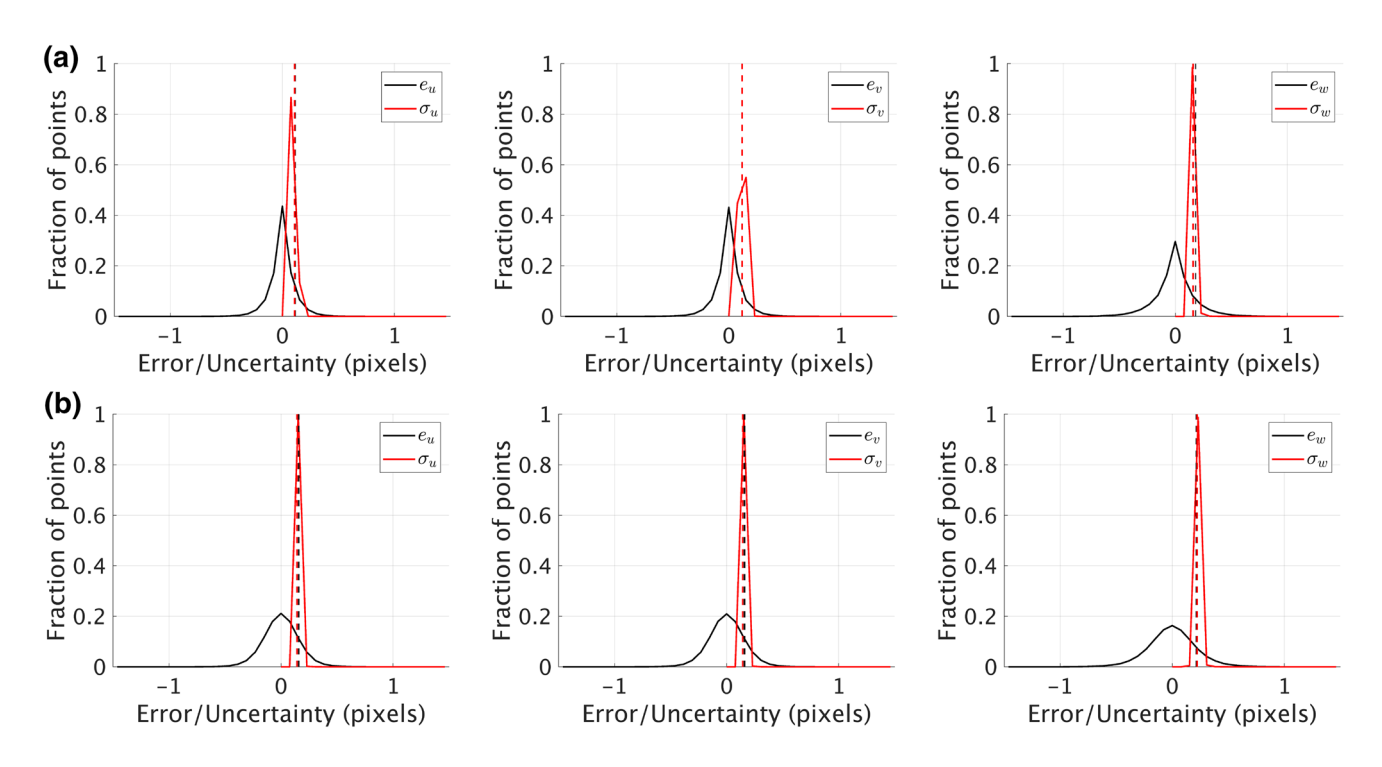


Fig. 7 Error and uncertainty histogram comparison for tracked velocity vectors in the synthetic vortex ring case with seeding density of 0.05 ppp for **a** triangulation- and **b** IPR-based reconstructions. The fraction of total number of measurement points is shown for each histogram bin

the displacement uncertainty model proposed by Eq. (11) for higher seeding densities with STB processing; however, these results show reasonable agreements between predicted and expected uncertainty values for the estimated velocity components.

3.4 Experimental validation: uncertainty prediction for laminar pipe flow

The current framework is also validated for a canonical laminar pipe flow experiment for a Reynolds number of 630. The



197 Page 14 of 18 Experiments in Fluids (2020) 61:197

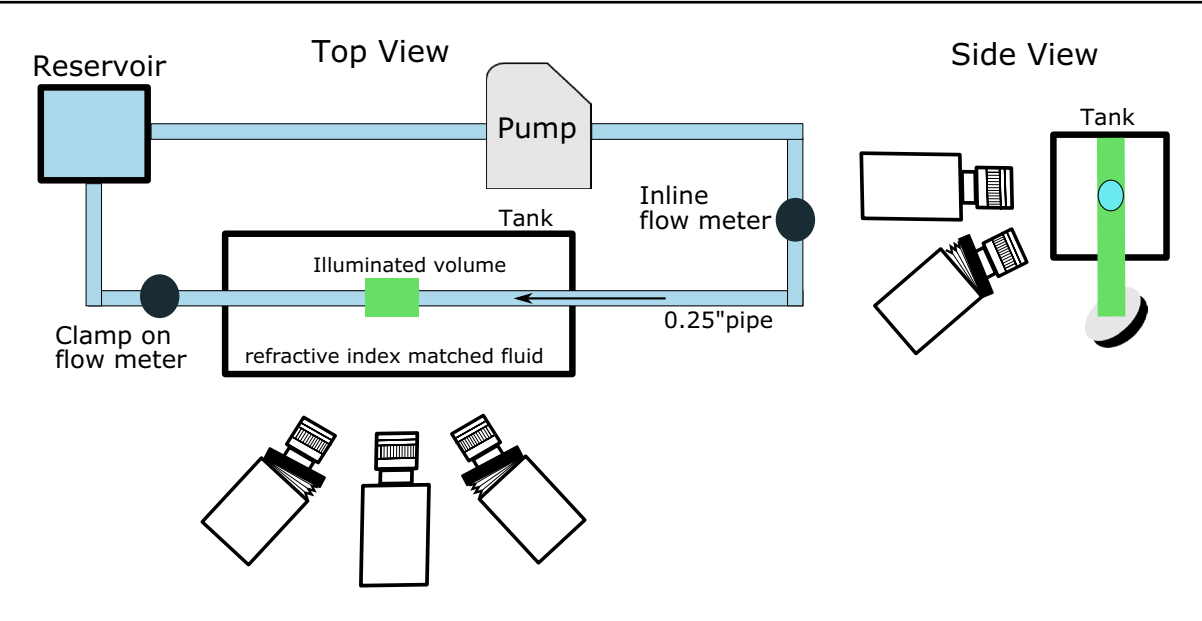


Fig. 8 Schematic of laminar pipe flow set-up showing the flow loop and camera arrangement

schematic of the experimental set-up is shown in Fig. 8. The flow loop consisted of a gear pump driving a steady flow rate of 0.17 L/min through a circular fluorinated ethylene propylene (FEP) tube of 0.25 inches inner diameter and 0.0625 inches thickness. Following Brindise et al. (2018), the working fluid inside the pipe was chosen as distilled water-urea (90:10) solution to closely match the refractive index of the FEP tube (1.344) and also maintain properties similar to water. The solution had a density of 1015 kg/m³, dynamic viscosity of 0.915×10^{-3} kg/m/s, and a refractive index of 1.3439. The tube was fully immersed in an acrylic tank filled with water-glycerol solution, which was also refractive index matched. The volumetric PTV measurement was performed using four Phantom Miro M340 cameras with three cameras at the same horizontal plane and one camera angled in the vertical plane, as shown in the side view of Fig. 8. The flow rate in the upstream and downstream of the pipe was measured using an ultrasonic flowmeter and the average flow rate was used to determine the theoretical velocity profile for Poiseuille's flow. The measurement volume was $9 \times 6.5 \times 6.5 \text{ mm}^3$ and was illuminated by a continuum Terra-PIV laser with appropriate optical set-up. The time-resolved measurements were taken at 6 kHz, and the image size was 640 × 624 pixels with an average magnification of 17.8 microns/pixel. Fluorescent particles with 24 microns diameter were used and the evaluated particle Stokes number St was 0.0005.

The reconstructed particle positions across all images are summed up in the cross-sectional view of the tube and a least-square circular fit is performed to fit a circle with size closest to the diameter of the tube. The fitted boundary is used to divide the cross-sectional area of the tube

in 20 × 20 bins and all measurements in streamwise direction as well as across 500 frames are averaged per bin to obtain the mean velocity profile shown in Fig. 9a. The mean velocity profile along the middle y_{in} -plane is compared with the theoretical solution in Fig. 9b. The expected theoretical velocity profile u_{true} for the measured flow rate is shown by the blue solid line. The velocity profiles are normalized by the maximum theoretical velocity (u_0) of 1.67 voxels/frame. The flow meter has a 1.1% uncertainty and its corresponding standard uncertainty $(\pm \sigma)$ is shown by the blue shaded region. The mean velocity profile obtained from particle tracks (for the triangulation case) is shown by the black solid line and the standard deviation of the velocity measurements in each bin is shown by the shaded gray region. The peak measured velocity reaches 94% of the theoretical maximum velocity. The standard deviation of the measured velocity is observed to increase in the depth direction moving away from the camera. The higher velocity standard deviation at $z_w/D = -0.5$ can be attributed to a higher calibration error due to initial misalignment between the pipe center and the calibration plane. The updated pipe boundary location (indepth direction) after volume self-calibration was aligned very close to the negative limit of the calibration plate traverse range and thus increasing the calibration uncertainty at that location. Overall, the mean velocity profile agreed with the expected parabolic profile of a laminar pipe flow.

The measured streamwise component of velocity (u) is compared with the theoretical expected velocity (u_{true}) and the distribution of velocity tracking error e_u and the estimated corresponding uncertainty σ_u is shown in Fig. 9c, d for the triangulation and IPR reconstruction cases, respectively. In both cases, the error distributions have a bias of



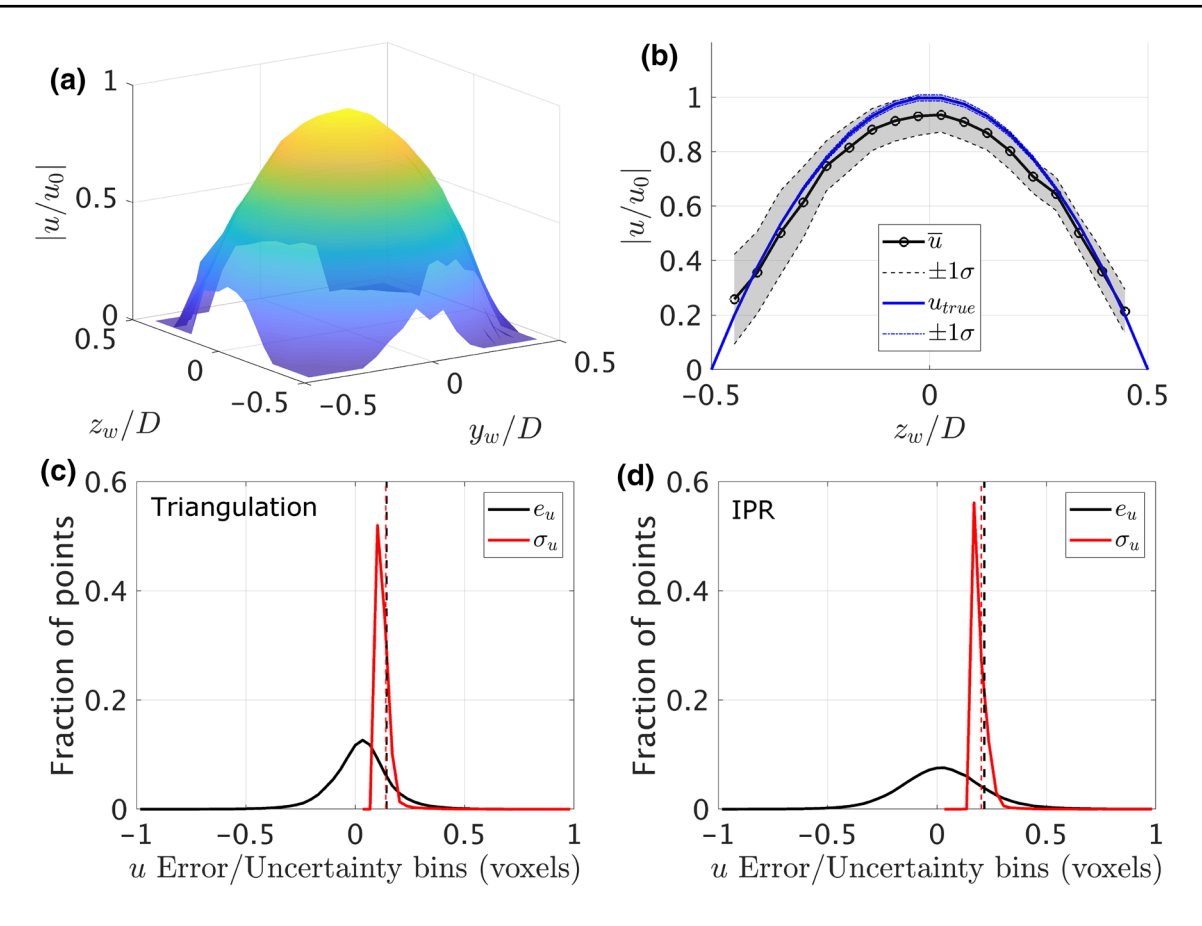


Fig. 9 The mean streamwise velocity profile for a 3D PTV measurement of a laminar pipe flow is shown in (a). The velocity profile is compared with the theoretical solution in (b). The error and estimated

uncertainty histogram are shown for triangulation-based reconstruction in (c) and for IPR-based reconstruction in (d)

about 0.03 pixels/frame. The predicted uncertainty values are distributed closely about the RMS error value. The RMS error and RMS uncertainty values match precisely at 0.14 pixels/frame for Fig. 9c. For Fig. 9d, the RMS error and uncertainty values are 0.22 pixels/frame and 0.20 pixels/ frame, respectively. The v component RMS uncertainty of 0.19 pixels/frame exactly matches the RMS error for the IPR case, but overpredicts the RMS error by 0.05 pixels/frame for the triangulation case. The w component of velocity, which corresponds to the depth direction, results in a higher RMS error of 0.44 pixels/frame and 0.57 pixels/frame for the triangulation and IPR reconstructions, respectively. The predicted uncertainties are 0.56 pixels/frame and 0.86 pixels/ frame for triangulation and IPR cases, respectively, indicating overprediction of standard uncertainty in the depth direction. The contribution of the calibration uncertainty $(\overline{\Sigma}_{\vec{a}^c})$ and particle image position uncertainty $(\overline{\Sigma}_{\vec{X}^c})$ to the overall uncertainty $(\overline{\Sigma}_{\vec{x}_{o}})$ is also analyzed for the experimental case. The $\overline{\Sigma}_{\overrightarrow{a}^c}$ term contributes on average to 25% of the total uncertainty, whereas the $\overline{\Sigma}_{\chi}$ term has 75% contribution. Thus, $\overline{\Sigma}_{\overrightarrow{X}}$ has a more significant contribution; however, the

calibration uncertainty contribution is higher for the experimental case compared to the synthetic case. Overall, for the experimental demonstration case, the predicted uncertainty using the current framework matches the expected uncertainty level with high accuracy for the *u* and *v* components, and reasonably matches the appropriate uncertainty level for the *w* velocity component.

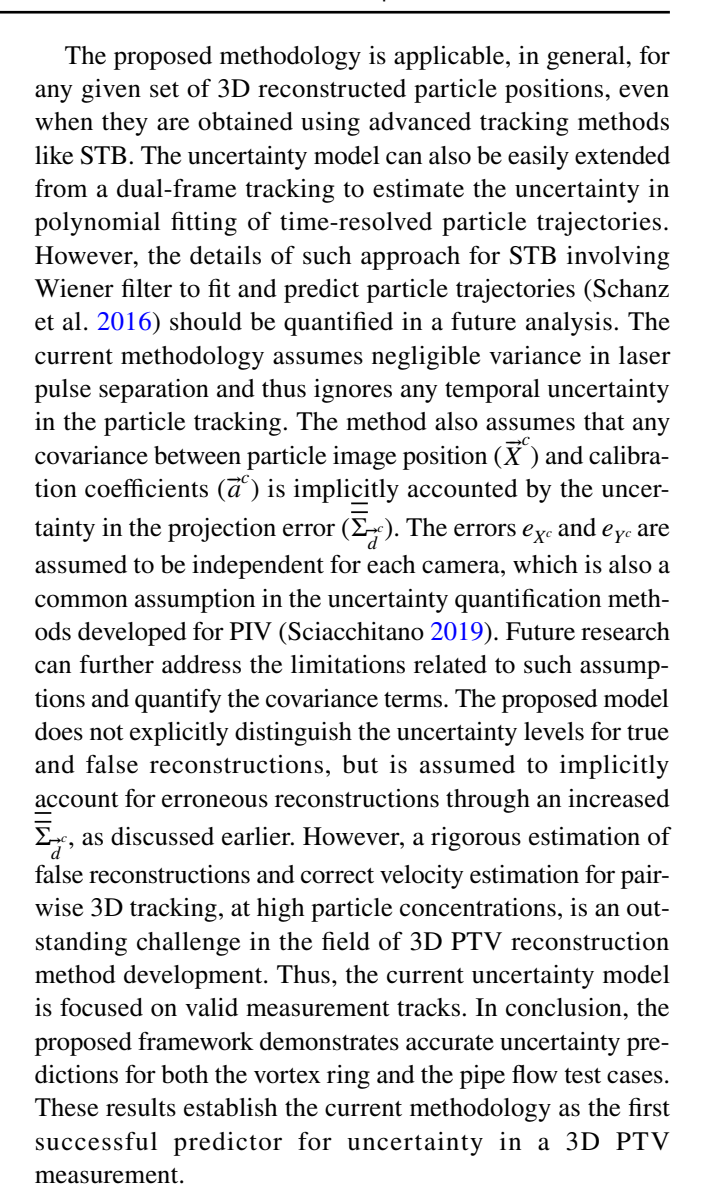
4 Conclusion

We proposed a comprehensive framework to predict the uncertainty in the reconstructed 3D particle positions in a volumetric PTV measurement and, subsequently, propagate the uncertainty in the tracked velocity estimates. The variance estimated from the histogram of the projection error provides the uncertainty bound on the particle image position and contributes to the uncertainty in the mapping function coefficients. The uncertainty on the reconstructed 3D position is obtained as a combination of the particle image position uncertainty and the mapping function coefficient uncertainty. The bias uncertainty on the reconstructed



particle positions due to the residual mean disparity is also considered. For the tracked velocity uncertainty, the uncertainty in the reconstructed particle positions is directly combined for each matching particle pair. The covariance between particle position error for paired particles in frame 1 and frame 2 is estimated using the correlation coefficient of the disparity error values for corresponding particles. Analysis with the synthetic vortex ring images showed good agreement between the RMS of the predicted uncertainties in x_w, y_w, z_w positions and the RMS error. The estimated uncertainty in the displacement field was within 0.04 voxels/ frame of the RMS error for both the vortex ring case and the experimental pipe flow case (u and v components). However, the w component uncertainty showed an overprediction of about 0.1–0.3 voxels/frame for the pipe flow case. Overall, the predicted uncertainties across all test cases are sharply distributed close to the RMS error values and showed strong sensitivity to the variation in RMS error, across a range of seeding densities.

The current analysis investigated the uncertainty prediction as a function of particle concentration, which is a primary error source in 3d PTV measurement. However, particle image size, shape, and image noise also affect the RMS error in such a measurement. A triangulation-based reconstruction uses the particle image information only for the 2D position estimation and the IPR method uses an OTF to estimate an average particle shape, which is not directly incorporated in the proposed uncertainty modeling. Hence, given the reconstruction methods, the particle image size and shape would primarily affect the accuracy in the particle image position estimation ($\overline{\Sigma}_{\overrightarrow{X}_{est}}^{c}$). The RMS error in particle image location estimation as a function of particle image size has been previously discussed in the literature (Cowen et al. 1997; Marxen et al. 2000; Brady et al. 2009). We expect a similar behavior for the position estimation error and its variance estimated from the least-square fit. Also, in the current uncertainty model, since the uncertainty in the disparity error $(\Sigma_{\stackrel{\rightarrow}{d}})$ has a more significant contribution in the $\overline{\Sigma}_{\chi}^{\text{c}}$ term, which in turn dominates the $\overline{\Sigma}_{\chi_w}$ uncertainty, we expect the current framework to be minimally affected by any variation in the particle image position fitting uncertainty $\overline{\Sigma}_{\overrightarrow{X}}^c$. In terms of image noise, higher noise leads to inaccuracy in triangulation and increases the fraction of ghost particles. An increase in triangulation error contributes to higher reprojection error uncertainty $\overline{\Sigma}_{d}^{\infty}$, which in turn should proportionally increase the uncertainty in the reconstructed position. The uncertainty prediction for the experimental case incorporates the effects of image noise and successful prediction for the pipe flow case demonstrates the capability of the current methodology to inherently consider any uncertainty due to image noise.



Acknowledgements This work is supported by the National Science Foundation's MRI program grant with award number 1725929.

References

Angioletti M, Nino E, Ruocco G (2005) CFD turbulent modelling of jet impingement and its validation by particle image velocimetry and mass transfer measurements. Int J Therm Sci 44(4):349–356. https://doi.org/10.1016/j.ijthermalsci.2004.11.010

Baek SJ, Lee SJ (1996) A new two-frame particle tracking algorithm using matching possibility. Exp Fluids 22:261–304

Bhattacharya S, Charonko JJ, Vlachos PP (2017) Stereo-particle image velocimetry uncertainty quantification. Meas Sci Technol 28(1):015301. https://doi.org/10.1088/1361-6501/28/1/015301

Bhattacharya S, Charonko JJ, Vlachos PP (2018) Particle image velocimetry (PIV) uncertainty quantification using moment of correlation (MC) plane. Meas Sci Technol 29(11):115301. https://doi.org/10.1088/1361-6501/aadfb4



- Boomsma A, Bhattacharya S, Troolin D, Pothos S, Vlachos P (2016) A comparative experimental evaluation of uncertainty estimation methods for two-component PIV. Meas Sci Technol 27(9):094006. https://doi.org/10.1088/0957-0233/27/9/094006
- Brady MR, Raben SG, Vlachos PP (2009) Methods for digital particle image sizing (DPIS): comparisons and improvements. Flow Meas Instrum 20(6):207–219. https://doi.org/10.1016/j.flowmeasinst.2009.08.001
- Brindise MC, Busse MM, Vlachos PP (2018) Density- and viscosity-matched newtonian and non-newtonian blood-analog solutions with PDMS refractive index. Exp Fluids 59(11):173. https://doi.org/10.1007/s00348-018-2629-6
- Brindise MC, Sean R, Dickerhoff B, Schnell S, Markl M, Saloner D, Rayz VL, Vlachos PP (2019) Multi-modality cerebral aneurysm haemodynamic analysis: in vivo 4D flow MRI, in vitro volumetric particle velocimetry and in silico computational fluid dynamics. J R Soc Interface. https://doi.org/10.1098/rsif.2019.0465
- Cardwell ND, Vlachos PP, Thole KA (2011) A multi-parametric particle-pairing algorithm for particle tracking in single and multiphase flows. Meas Sci Technol 22(10):105406. https://doi. org/10.1088/0957-0233/22/10/105406
- Charonko JJ, Vlachos PP (2013) Estimation of uncertainty bounds for individual particle image velocimetry measurements from crosscorrelation peak ratio. Meas Sci Technol 24(6):065301. https://doi. org/10.1088/0957-0233/24/6/065301
- Cierpka C, Lütke B, Kähler CJ (2013) Higher order multi-frame particle tracking velocimetry. Exp Fluids 54(5):1533. https://doi.org/10.1007/s00348-013-1533-3
- Coleman HW, Glenn Steele W (2009) Experimentation, validation, and uncertainty analysis for engineers. Wiley, Hoboken. https://doi. org/10.1002/9780470485682
- Cowen EA, Monismith SG, Cowen EA, Monismith SG (1997) A hybrid digital particle tracking velocimetry technique. Exp Fluids 22(3):199–211. https://doi.org/10.1007/s003480050038
- Elsinga GE, Scarano F, Wieneke B, van Oudheusden BW (2006) Tomographic particle image velocimetry. Exp Fluids 41(6):933–947. https://doi.org/10.1007/s00348-006-0212-z
- Ferreira CS, Van Bussel G, Van Kuik G (2007) 2D CFD simulation of dynamic stall on a vertical axis wind turbine: verification and validation with PIV measurements. In: Collection of technical papers—45th AIAA aerospace sciences meeting, vol 23, pp 16191–201. https://doi.org/10.2514/6.2007-1367
- Ford MD, Nikolov HN, Milner JS, Lownie SP, DeMont EM, Kalata W, Loth F, Holdsworth DW, Steinman DA (2008) PIV-measured versus CFD-predicted flow dynamics in anatomically realistic cerebral aneurysm models. J Biomech Eng. https://doi.org/10.1115/1.29007 24
- Fuchs T, Hain R, Kähler CJ (2016) Double-frame 3D-PTV using a tomographic predictor. Exp Fluids 57(11):174. https://doi.org/10.1007/s00348-016-2247-0
- Fuchs T, Hain R, Kähler CJ (2017) Non-iterative double-frame 2D/3D particle tracking velocimetry. Exp Fluids 58(9):119. https://doi.org/10.1007/s00348-017-2404-0
- Gavin H (2011) The Levenberg–Marquardt method for nonlinear least squares curve-fitting problems. Department of Civil and Environmental Engineering, Duke University, Durham, pp 1–15
- Guezennec YG, Brodkey RS, Trigui N, Kent JC (1994) Algorithms for fully automated three-dimensional particle tracking velocimetry. Exp Fluids 17(4):209–219. https://doi.org/10.1007/BF00203039
- Lei Y-C, Tien W-H, Duncan J, Paul M, Ponchaut N, Mouton C, Dabiri D, Rösgen T, Hove J (2012) A vision-based hybrid particle tracking velocimetry (PTV) technique using a modified cascade correlation peak-finding method. Exp Fluids 53(5):1251–1268. https://doi.org/10.1007/s00348-012-1357-6

- Li D, Zhang Y, Sun Y, Yan W (2008) A multi-frame particle tracking algorithm robust against input noise. Meas Sci Technol 19(10):105401. https://doi.org/10.1088/0957-0233/19/10/105401
- Maas HG, Gruen A, Papantoniou D (1993) Particle tracking velocimetry in three-dimensional flows. Exp Fluids 15(2):133–146. https://doi. org/10.1007/BF00190953
- Malik NA, Dracos Th, Papantoniou DA (1993) Particle tracking velocimetry in three-dimensional flows—Part II: particle tracking. Exp Fluids 15(4–5):279–294. https://doi.org/10.1007/BF00223406
- Marxen M, Sullivan PE, Loewen MR, Jähne B (2000) Comparison of gaussian particle center estimators and the achievable measurement density for particle tracking velocimetry. Exp Fluids 29(2):145–153. https://doi.org/10.1007/s003489900085
- Mikheev AV, Zubtsov VM (2008) Enhanced particle-tracking velocimetry (EPTV) with a combined two-component pair-matching algorithm. Meas Sci Technol 19(8):085401
- Ohmi K, Li H-Y (2000) Particle-tracking velocimetry with new algorithms. Meas Sci Technol 11(6):603–616. https://doi.org/10.1088/0957-0233/11/6/303
- Okamoto K, Hassan YA, Schmidl WD (1995) New tracking algorithm for particle image velocimetry. Exp Fluids 19(5):342–347. https:// doi.org/10.1007/BF00203419
- Pereira F, Stüer H, Graff EC, Gharib M (2006) Two-frame 3D particle tracking. Meas Sci Technol 17(7):1680–1692. https://doi.org/10.1088/0957-0233/17/7/006
- Rajendran LK, Bane SPM, Vlachos PP (2019) Uncertainty amplification due to density/refractive-index gradients in volumetric PTV and BOS experiments. ArXiv Preprint ArXiv:1910.09379
- Schanz D, Gesemann S, Schröder A, Wieneke B, Novara M (2013) Nonuniform optical transfer functions in particle imaging: calibration and application to tomographic reconstruction. Meas Sci Technol 24(2):024009. https://doi.org/10.1088/0957-0233/24/2/024009
- Schanz D, Gesemann S, Schröder A (2016) Shake-the-box: lagrangian particle tracking at high particle image densities. Exp Fluids 57(5):70. https://doi.org/10.1007/s00348-016-2157-1
- Sciacchitano A (2019) Uncertainty quantification in particle image velocimetry. Meas Sci Technol. https://doi.org/10.1088/1361-6501/ab1db8
- Sciacchitano A, Wieneke B, Scarano F (2013) PIV uncertainty quantification by image matching. Meas Sci Technol 24(4):045302. https://doi.org/10.1088/0957-0233/24/4/045302
- Sciacchitano A, Neal DR, Smith BL, Warner SO, Vlachos PP, Wieneke B, Scarano F (2015) Collaborative framework for PIV uncertainty quantification: comparative assessment of methods. Meas Sci Technol 26(7):074004. https://doi.org/10.1088/0957-0233/26/7/074004
- Soloff SM, Adrian RJ, Liu ZC (1997) Distortion compensation for generalized stereoscopic particle image velocimetry. Meas Sci Technol 8(12):1441–1454
- Stitou A, Riethmuller ML (2001) Extension of PIV to super resolution using PTV. Meas Sci Technol 12(9):1398
- Takehara K, Adrian RJ, Etoh GT, Christensen KT (2000) A Kalman tracker for super-resolution PIV. Exp Fluids 29(1):S034–41. https://doi.org/10.1007/s003480070005
- Timmins BH, Wilson BW, Smith BL, Vlachos PP (2012) A method for automatic estimation of instantaneous local uncertainty in particle image velocimetry measurements. Exp Fluids. https://doi.org/10.1007/s00348-012-1341-1
- Van Gent PL, Michaelis D, Van Oudheusden BW, Weiss P-É, De Kat R, Laskari A, Jeon YJ et al (2017) Comparative assessment of pressure field reconstructions from particle image velocimetry measurements and lagrangian particle tracking. Exp Fluids 58:33. https://doi.org/10.1007/s00348-017-2324-z
- van Ooij P, Guédon A, Poelma C, Schneiders J, Rutten MCM, Marquering HA, Majoie CB, vanBavel E, Nederveen AJ (2012) Complex flow patterns in a real-size intracranial aneurysm phantom: phase contrast mri compared with particle image velocimetry and



- computational fluid dynamics. NMR Biomed 25(1):14–26. https://doi.org/10.1002/nbm.1706
- Wieneke B (2008) Volume self-calibration for 3D particle image velocimetry. Exp Fluids 45:549–556. https://doi.org/10.1007/s00348-008-0521-5
- Wieneke B (2013) Iterative reconstruction of volumetric particle distribution. Meas Sci Technol 24(2):024008. https://doi.org/10.1088/0957-0233/24/2/024008
- Wieneke B (2015) PIV uncertainty quantification from correlation statistics. Meas Sci Technol 26(7):074002. https://doi.org/10.1088/0957-0233/26/7/074002
- Wu J-Z, Ma H-Y, Zhou M-D (2006) Vorticity and vortex dynamics. Springer, Berlin, Heidelberg. https://doi.org/10.1007/978-3-540-29028-5
- Xue Z, Charonko JJ, Vlachos PP (2014) Particle image velocimetry correlation signal-to-noise ratio metrics and measurement uncertainty quantification. Fluid Dyn Meas Sci Technol 25(11):115301. https://doi.org/10.1088/0957-0233/25/11/115301
- Xue Z, Charonko JJ, Vlachos PP (2015) Particle image pattern mutual information and uncertainty estimation for particle image velocimetry. Meas Sci Technol 26(7):074001. https://doi.org/10.1088/0957-0233/26/7/074001

Publisher's Note Springer Nature remains neutral with regard to jurisdictional claims in published maps and institutional affiliations.

